SIMULATIONS OF DEUTERIUM–TRITIUM EXPERIMENTS IN TFTR

R.V. BUDNY, M.G. BELL, H. BIGLARI, M. BITTER, C.E. BUSH, C.Z. CHENG,
E.D. FREDRICKSON, B. GREK, K.W. HILL, H. HSUAN, A.C. JANOS, D.L. JASSBY,
D.W. JOHNSON, L.C. JOHNSON, B. LeBLANC, D.C. McCUNE, D.R. MIKKELSEN,
H.K. PARK, A.T. RAMSEY, S.A. SABBAGH, S.D. SCOTT, J.F. SCHIVELL, J.D. STRACHAN,
B.C. STRATTON, E.J. SYNAKOWSKI, G. TAYLOR, M.C. ZARNSTORFF, S.J. ZWEBEN
Princeton Plasma Physics Laboratory,
Princeton University,
Princeton, New Jersey,
United States of America

ABSTRACT. A transport code (TRANSP) is used to simulate future deuterium–tritium (DT) experiments in TFTR. The simulations are derived from 14 TFTR DD discharges, and the modelling of one supershot is discussed in detail to indicate the degree of accuracy of the TRANSP modelling. Fusion energy yields and α particle parameters are calculated, including profiles of the α slowing down time, the α average energy, and the Alfvén speed and frequency. Two types of simulation are discussed. The main emphasis is on the DT *equivalent*, where an equal mix of D and T is substituted for the D in the initial target plasma, and for the D^0 in the neutral beam injection, but the other measured beam and plasma parameters are unchanged. This simulation does not assume that α heating will enhance the plasma parameters or that confinement will increase with the addition of tritium. The maximum relative fusion yield calculated for these simulations is $Q_{DT} \sim 0.3$, and the maximum α contribution to the central toroidal β is $\beta_\alpha(0) \sim 0.5\%$. The stability of toroidicity induced Alfvén eigenmodes (TAE) and kinetic ballooning modes (KBM) is discussed. The TAE mode is predicted to become unstable for some of the simulations, particularly after the termination of neutral beam injection. In the second type of simulation, empirical supershot scaling relations are used to project the performance at the maximum expected beam power. The MHD stability of the simulations is discussed.

1. INTRODUCTION

Experiments using a mix of deuterium and tritium (DT) are planned for TFTR to study plasma conditions near breakeven ($Q_{DT} \equiv$ DT fusion power/NBI power $= 1$) and to study the effects of fusion α particles. The purpose of this paper is to give examples of the fusion energy yields and the α parameters which can be expected from the DT experiments in TFTR. Some simulations of DT plasmas in TFTR have already been published [1–5]. This paper discusses simulations calculated with the TRANSP transport code [6–8]. Detailed results and profiles are given for use in studying α particle effects and plasma stability.

The TRANSP Monte Carlo fast ion model [6] was recently extended to include the fast fusion products from the reactions

$$D + D \rightarrow T + p \tag{1a}$$

$$D + D \rightarrow {}^3He + n \tag{1b}$$

$$D + T \rightarrow {}^4He + n \tag{1c}$$

Monte Carlo births of T, ^{3}He and ^{4}He (α) are performed using spatially 2-D fusion reaction rate data (beam–beam + beam–target + thermonuclear) computed in the preceding time step. The fusion products are launched in the (rotating) plasma frame with the appropriate energy (e.g. 3.5 MeV for the α particles). Their orbits, their slowing down and their heating of the thermal plasma are calculated using the same methods employed in modelling the fast ions from neutral beam injection (NBI). The model takes into account non-zero orbit width effects and Larmor radius effects, but magnetic field ripple effects are not included.

The fusion products slow down and pitch angle scatter on thermal plasma species (electrons, ions and impurities). They are treated as thermalized when they slow down to the average energy of the local thermal ion population ($\frac{3}{2} kT_i$). Collisional coupling between fast ion species (e.g. beam–beam and beam–α collisional effects) is not computed. Effects which are included in the Monte Carlo model of injected fast ions but not yet in the fusion product simulation are atomic physics effects (e.g. charge exchange of par-

tially slowed α particles and/or ionization of neutral atoms by α particles) and accumulation of thermalized fusion products.

The discharges which should show the largest effects from the α particles are those with a high DT fusion rate (the α production rate), with a long slowing down time for the α particles, and with a high plasma current to confine the α particles as they thermalize [4]. The fusion rate increases with the products $n_{thermal}^2$, $n_{beam}n_{thermal}$ and n_{beam}^2. The α slowing down time increases approximately as $T_e^{1.5}/n_e$.

A number of TFTR discharges, listed in Table I, were used for deriving the DT simulations. Most of these are supershots [9], chosen because they have the highest neutron rates observed in TFTR. The list includes the discharges with the highest DD fusion rates (55806, 55804 and 53848, with 5.0, 4.6 and

4.4×10^{16} s^{-1}, respectively). Three of them had the highest values for Q_{DD} ($\equiv$ DD fusion power/NBI power). The DT simulations were also derived from an L-mode discharge with sawteeth, and from a discharge with deuterium pellets injected before NBI to compare their yields with those from DT supershots. Deuterium was the dominant ion species for all these discharges.

TRANSP is generally run in a mode which is partly phenomenological and partly predictive. The phenomenological or empirical part consists of using as input measured plasma parameters, such as the total current, the boundary at the last closed flux surface, and temperature and density profiles. There is considerable flexibility in the options for inputting the profiles. For instance, the electron temperature can be input as a profile of electron cyclotron emission (ECE) versus

TABLE I. TFTR DISCHARGES USED FOR DT EQUIVALENT SIMULATIONS, AND SUMMARY OF PEAK RESULTS

					Measured	TRANSP results			
Discharge	Type	I_p (MA)	P_{NB} (MW)	χ_i	Q_{DD} (10^3)	Q_{DT}/Q_{DD}	Ratio	$\beta_\alpha(0)$ (%)	$\langle\beta_\alpha\rangle$ (10^4)
26627	Supershot	0.85	10.6	$2\chi_e$	0. 91	0.206/0.00103	201	0.10	1.1
35782	Supershot	1.4	22.0	CHERS	1.62	0.297/0.00181	164	0.28	4.2
37081	Supershot	1.6	30.4	CHERS	1.50	0.234/0.00154	152	0.28	3.2
37083	Supershot	1.6	30.2	CHERS	1.36	0.239/0.00147	163	0.25	3.1
37084	Supershot	1.6	30.2	CHERS	1.47	0.246/0.00152	162	0.20	3.1
37085	Supershot	1.6	25.0	CHERS	1.59	0.292/0.00181	161	0.28	2.9
45950[a]	L-mode	2.0	11.4	CHERS	0.41	0.098/0.00041	239	0.03	0.4
47394[b]	Supershot	1.6	24.3	$1\chi_e$	1.83	0.255/0.00168	152	0.02	2.7
53793[c]	Supershot	1.7	26.2	$2\chi_e$	1.43	0.258/0.00171	151	0.30	4.6
53848[c]	Supershot	1.6	25.5	$2\chi_e$	1.74	0.291/0.00183	159	0.55	6.0
55053	Pellets	2.0	22.8	CHERS	0.84	0.124/0.00103	120	0.14	1.4
55804	Supershot	1.84	32.5	$2\chi_e$	1.66	0.291/0.00196	165	0.32	4.3
55806	Supershot	1.6	32.5	CHERS	1.81	0.298/0.00188	156	0.33	4.7
55851	Supershot	1.6	24.6	CHERS	1.81	0.275/0.00159	173	0.33	3.9

[a] Sawteeth during NBI.
[b] Ended with a disruption and poorly diagnosed, so the modelling is suspect.
[c] The quoted Q values occur just before the mild compression in major and minor radius; the quoted $\beta_\alpha(0)$ and $\langle\beta_\alpha\rangle$ values occur during the compression.

frequency and time, or it can be input as concatenations of Thomson scattering (TVTS) profiles versus the major radius at different times.

Many parameters can be predicted by TRANSP. For instance, the ion temperature can be predicted by assuming that the ion thermal conductivity χ_i is a multiple of the electron thermal conductivity χ_e. This modelling assumption is useful when T_i has not been measured, since it has been found that $\chi_i = (1 \text{ or } 2)\chi_e$ predicts T_i profiles which are in approximate agreement with measurements in fully diagnosed supershots. Also the impurity ion temperature T_{imp} is predicted by TRANSP from the hydrogenic ion temperature T_i. The method is described in the Appendix. Various other measurements can be predicted or simulated with TRANSP; for instance, chordal integrals of the electron density and the visible bremsstrahlung emission can be simulated.

A sawtooth model, based on Kadomtsev mixing [10], is available in TRANSP. Sawtooth crash times are specified as inputs, and TRANSP computes the mixing of the current and fast particles (beam ions and fusion products). The sawtooth model was used for some of the simulations and has consequences for the α parameters.

This paper concentrates on TRANSP results derived from the supershot 55851. This discharge was selected since it maintained a high DD fusion rate for a long duration and had a plasma current high enough (1.6 MA) for good α confinement, a high central T_e for low electron drag, and extensive diagnostic measurements. Also, this discharge was the MHD free plasma with the largest Q_{DD} measured in TFTR.

Sections 2–4 give results from the modelling of discharge 55851. Detailed comparisons of the TRANSP results with measurements are discussed in Section 2 in order to indicate the degree of accuracy of the modelling. Alternative modelling assumptions are discussed to indicate the sensitivity to the assumptions. In particular, the neutron emission profile is important since, in the DT simulations, it gives the source rate of the fusion α particles.

Calculations of profiles of the pressure and of the MHD-q, q_ψ, needed for the MHD stability analysis, are given. The ideal MHD stability is discussed in Section 3. The discharge is calculated to be stable to Mercier modes [11] and marginally stable to low-n and high-n modes. A summary of the TRANSP predictions for fusion product parameters from the DD reactions is given in Section 4. As expected, the parameters are very small compared with the simulated DT parameters.

Two types of DT simulations are then discussed. The main emphasis is on a conservative simulation, called the DT *equivalent* of actual DD discharges. The second type of simulation is a more optimistic extrapolation of the best present performance to the highest expected NBI power. The DT equivalent simulations are discussed in Section 5 and are compared with previously published simulations for JET [12, 13]. Section 6 gives the fusion yields and the α parameters for the DT equivalent of discharge 55851. Section 7 presents the results for the DT extrapolation.

For both types of simulations, the measured plasma and NBI parameters from DD discharges are used. The relative D and T densities in the initial plasma, and in the D^0 and T^0 beams are assumed to be equal. For the DT equivalent, the measured n_e, T_e, T_i and toroidal rotation profiles are used, together with the measured Z_{eff}, NBI powers, voltages, and full and half energy fractions. For the DT extrapolation, the NBI parameters and the plasma current, temperatures and densities are scaled up.

The collective α induced TAE and KBM instabilities are discussed in Section 8. They are predicted to be marginally unstable for the DT equivalent simulation. For instance, DT equivalent simulations are predicted to pass through the TAE unstable region after termination of NBI. Section 9 gives a summary of the paper.

2. TRANSP MODELLING OF SUPERSHOT 55851

The major and minor radii of this supershot were R = 2.45 m and a = 0.8 m, with a toroidal field B_{TF} = 5.1 T and $q_\psi(a)$ = 5.5. A lithium pellet was injected into the target plasma early (at 2.0 s) to improve the plasma performance [14]. Lithium pellets reduce the carbon concentration in supershots, apparently by coating the limiter, reducing carbon sputtering. The NBI power was 25 MW. The total current I_p was increased in the early phase of NBI, as shown in Fig.1(a). This increase was programmed in an attempt to improve the MHD stability. This discharge, like most supershots with plasma currents below about 1.8 MA, did not have sawteeth during the NBI phase. The normalized toroidal β, defined by

$$\beta_{norm} \equiv \frac{\langle \beta_{tor} \rangle}{I_p/(aB_{TF})} \tag{2}$$

reached 2.25. $\langle\ \rangle$ designates the volume average, and β_{tor}, I_p, a and B_{TF} are in %, MA, m and T. The peak
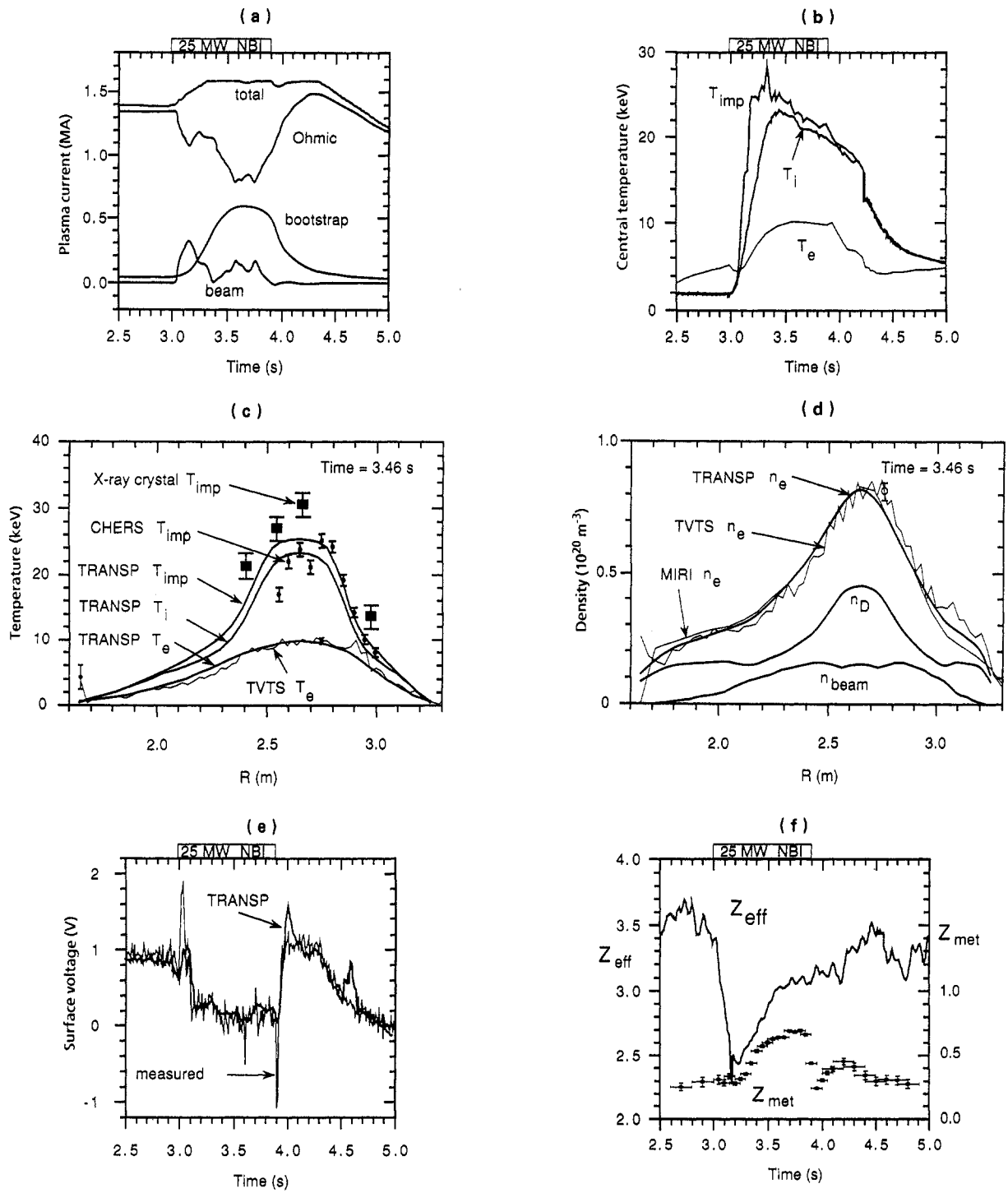
FIG. 1. TRANSP results and measurements for supershot 55851. (a) Components of the plasma current versus time. The total current was measured and input into TRANSP as a boundary condition. The beam driven and bootstrap currents are calculated in TRANSP from the beam deposition and total pressure profiles. The relative amounts of these non-inductive currents are typical of those calculated for supershots.
(b) Central values of the temperatures versus time. T_e is computed in TRANSP by symmetrizing the smoothed time dependent second harmonic ECE, which was cross-calibrated by the Thomson scattering profile at 3.46 s. T_{imp} is fitted by TRANSP using the time dependent CHERS measurements. The effects of sawteeth in the pre- and post-NBI plasma are shown. (c) Temperature profiles and measurements at the TVTS time. The TVTS profile is shown. T_e is derived from ECE, measured by GPC, cross-calibrated to TVTS, and symmetrized by in/out averaging. T_{imp} is fitted by TRANSP using the CHERS measurements from the magnetic axis out to larger major radii. The T_{imp} profile measured from Doppler broadening of iron X-ray lines is shown for comparison. Error bars for the measurements are also shown. (d) Density profiles and measurements at the TVTS time. The TVTS profile is scaled in magnitude so that the peak density is that measured by MIRI. The TRANSP n_e profile is calculated by symmetrizing the smoothed MIRI profile. The thermal deuterium density n_D and the beam density n_{beam} are cal-

(g)

(h)

(i)

(j)

(k)

(l)
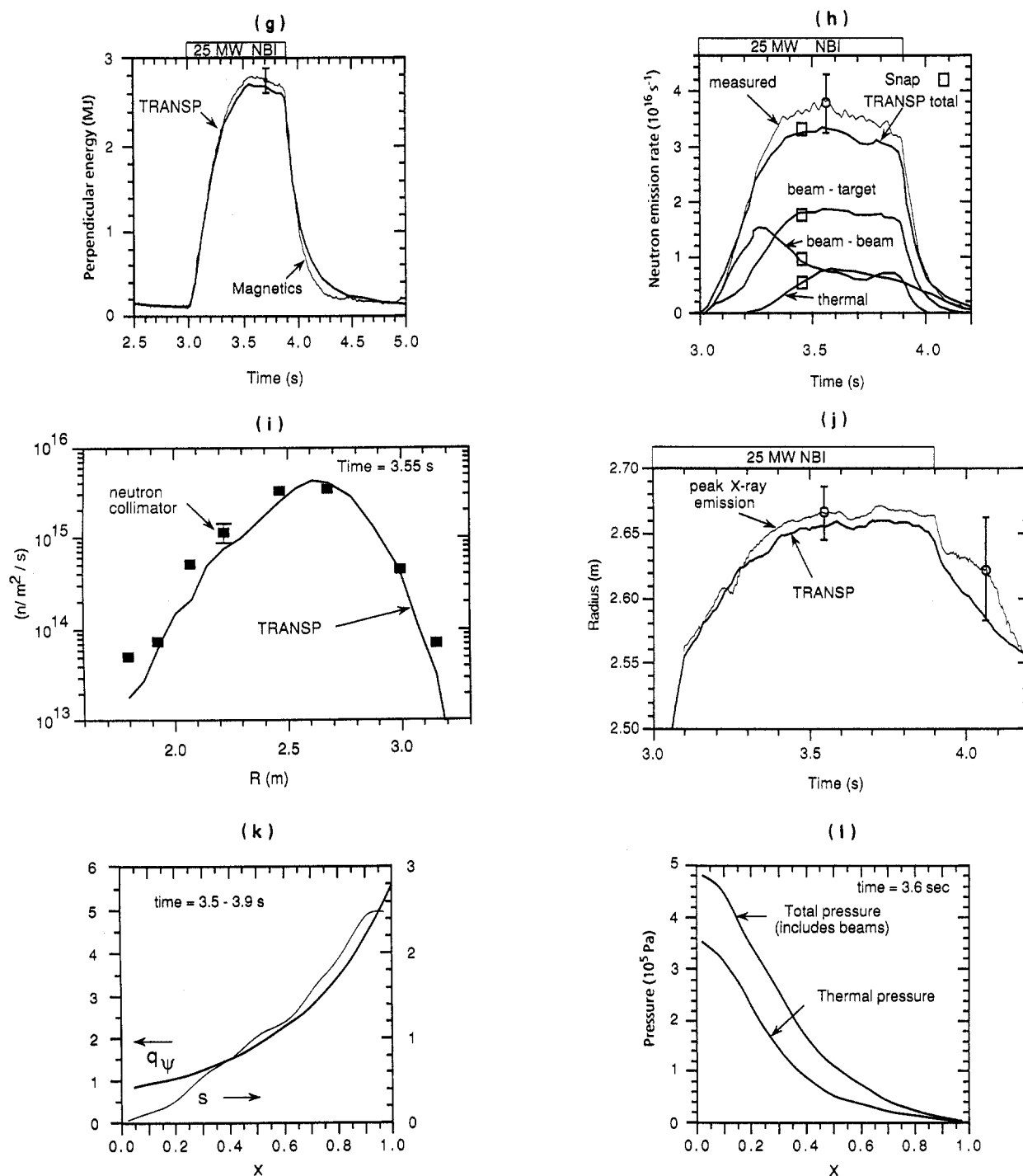
culated in TRANSP. (e) Surface voltage computed in TRANSP using neoclassical resistivity and beam driven and bootstrap currents, and compared with measured values. The errors on the measured values are less than ±0.04 V during quiescent periods (when dE/dt is small). (f) Z_{eff} computed from the measured visible bremsstrahlung, and Z_{met} (the contribution from Cr, Fe and Ni to Z_{eff}, measured by PHA) versus time. (g) Comparison of the predicted and measured perpendicular energy. The experimental errors for the measurement are ±150 kJ. (h) Total neutron emission rate compared with the measured value and the calculated beam–target, thermonuclear and beam–beam components versus time. The absolute error bars for the measurement are ±14%. Results from a steady state calculation using SNAP are shown. (i) Comparison of the simulated and measured neutron emission along vertical chords. The experimental errors are estimated to be ±20% near the peak, and larger in the inner and outer edges where the measured values are comparable to the scattered signal. (j) Computed location of the magnetic axis compared with the location of the region of maximum soft X-ray emission. The errors become larger after NBI. (k) Profiles of q_ψ and shear. The profiles do not vary appreciably between 3.5 and 3.9 s. (l) Profiles of the thermal and the total pressure.

value of β_{norm} is below the highest value achieved in supershots (2.7). The total energy confinement time reached a peak of 0.17 s around the time of maximum neutron emission.

For the TRANSP modelling of this discharge, various combinations of inputs for the temperatures were investigated. For instance, the electron temperature T_e was derived either from an absolutely calibrated, time dependent profile of first harmonic ECE measured by a radiometer [15] or from the time dependent profile of second harmonic ECE measured by a grating polychromator (GPC) [16]. In the latter case, the profile was cross-calibrated either by the second harmonic ECE measured with a Michelson interferometer [17] or by the TVTS profile [18] at 3.46 s. The central electron temperatures from the first two methods are about 15% higher than the values from the GPC cross-calibrated by TVTS, peaking above 11 keV. Differences of this magnitude are typically measured in supershots with high T_e (above about 8 keV).

All three derivations of T_e were modelled in different TRANSP runs. Comparisons of the modelling results with other measured parameters could not definitively exclude these alternative derivations. We indicate the sensitivity of our results to the assumptions about T_e and focus on the derivation using the GPC cross-calibrated by TVTS.

In the usual TRANSP modelling of supershots, the hydrogenic ion temperature T_i is fitted to measured temperature profiles of impurity ions. The impurity temperature T_{imp} is higher than T_i, and TRANSP was modified, as discussed in the Appendix, to estimate this difference. We modelled these corrections by fitting T_{imp} to the time dependent temperatures derived from charge exchange recombination spectroscopy (CHERS) [19] of emission from the $n = 8 \rightarrow n = 7$ transition in the hydrogen-like carbon impurity. These measurements were available only for the NBI phase of the discharge, so the assumption $\chi_i = 2\chi_e$ was used for the Ohmic phases. The central values of the TRANSP results for T_{imp} and T_i are shown in Fig. 1(b). The differences are relatively large at the start of NBI and decrease with time.

Time dependent profiles of T_{imp} were also calculated from measurements with an X-ray crystal spectrometer [20] of Doppler broadening of the resonance K_α emission from the helium-like iron impurity. Comparisons of the computed and measured temperature profiles at the TVTS time are shown in Fig. 1(c). The differences between the two measurements of T_{imp} shown here are atypically large and are smaller at later times in the discharge.

The toroidal rotation velocity of carbon was measured by CHERS and input into TRANSP as the rotation velocity of the thermal plasma. This velocity is relatively large (peaking at 5×10^5 m/s), even though NBI was approximately balanced, with equal co- and counter-tangential injection (relative to the direction of the plasma current).

The electron density was smoothed and symmetrized from the time dependent Abel inverted profiles measured by a ten-chord far infrared interferometer system [21] (MIRI). A comparison of the measured and calculated profiles at the TVTS time are shown in Fig. 1(d).

The surface voltage was calculated using neoclassical resistivity and the beam driven and bootstrap currents [22]. The result compares well with the measured value, as shown in Fig. 1(e). For the modelling using the higher T_e derived from the ECE measured by GPC, the agreement between the measured and calculated voltage was not as good in the Ohmic phase. Z_{eff} was calculated from the visible bremsstrahlung signal, and the result is shown in Fig. 1(f). The impurity radiation was measured with a multichannel grazing incidence spectrometer [23]. The dominant impurity in this discharge was carbon. The metallic contribution to Z_{eff}, Z_{met}, was measured with X-ray pulse height analysis (PHA) [24] and is shown as well.

Much of the increase in Z_{eff} during NBI is due to the increasing concentration of metallic impurities. Since TRANSP allows only one impurity species, the impurity was chosen to have $Z = 7.8$ instead of 6. This gives the correct depletion of the deuterium density corresponding to the measured Z_{eff} and Z_{met} around the time of maximum neutron emission. The calculated neutron emission rate depends sensitively on the D depletion. The hydrogenic recycling rate, which was input into TRANSP, was computed from five chordal signals of D_α emission using the 3D neutrals code DEGAS [25].

The perpendicular energy calculated by TRANSP is compared with the diamagnetically measured value in Fig. 1(g). The measured value was shifted up by 80 kJ to match the calculated values in the pre-NBI phase, where the measured value results from the subtraction of two measured quantities of comparable magnitude. TRANSP modelling using the higher T_e from ECE yielded perpendicular energies which were also in good agreement with the measured values. TRANSP modelling using the usual assumptions, where T_i instead of T_{imp} is fitted to the ion temperature measurements, yielded a peak perpendicular energy that is 100 kJ higher than the values obtained with the modelling presented here using the T_{imp} correction.

The calculated DD neutron emission rates are shown in Fig. 1(h). The total rate is within the absolute error bars of the measurements from a calibrated neutron diagnostic [26]. The beam–target contribution is 55% of the total rate. An independent calculation of the neutron rates was done with the 1D, time independent code SNAP [27] and the results are also shown in Fig. 1(h).

The TRANSP modelling using the usual assumptions, with T_i fitted to the impurity ion temperature measurements, yielded a peak neutron rate that is approximately 5% higher. TRANSP modelling using the higher T_e values from ECE yielded neutron emission rates which were again approximately 5% higher. The sensitivity of the modelling to the assumed fusion cross-section fits was investigated. Until recently, the fits of Duane [28] had been used in TRANSP. When the more recent fits of Bosch and Hale [29] were used, the total neutron rate decreased by about 5%.

An array of independently calibrated collimated neutron detectors [30] was also used to measure neutron emission rates. The chord integrated signals were simulated with TRANSP. The simulated rates are consistent with the measured rates, as shown in Fig. 1(i). The collimators are separated by approximately 0.2 m in major radius, so this comparison is not a precise measurement of the neutron emitting profile. The raw data from the collimated detectors include contributions from neutrons scattered from the tokamak and the surrounding structure, which have been estimated and subtracted from the measurement. The relative error from this contribution is higher near the edge of the plasma, where it is comparable to the net result. A more precise indication of the plasma centre is given by the location of the peak of the soft X-ray emission [31, 32]. This is compared with the TRANSP calculation in Fig. 1(j), and agrees to within several centimetres.

The Kadomtsev sawtooth model was used in the modelling of the pre- and post-NBI sawteeth. This alters the plasma current and raises $q_\psi(0)$ to 1 at the sawteeth events. Profiles of q_ψ and of the shear, defined as

$$s \equiv \frac{\ln q_\psi}{\ln x} \qquad (3)$$

are shown in Fig. 1(k). The profiles are plotted versus the normalized toroidal flux co-ordinate, x is the square root of the toroidal flux normalized to the value at the plasma boundary. The value of this variable is very

close to the normalized minor radius (r/a). Profiles of the thermal and total pressure (beam plus thermal) are shown in Fig. 1(l).

3. MHD ACTIVITY AND STABILITY OF SUPERSHOT 55851

There was no observed coherent MHD activity in this discharge. In contrast, very similar discharges developed severe MHD problems as early as 0.3 s after the start of NBI; the MHD modes in these cases were (m,n) = (2,1) and (3,2) modes [33]. The onset of these modes coincided with a severe degradation of the confinement and the neutron production rate. These modes are thought to be resistive in nature because their growth rates are slow compared to the ideal MHD time-scales. It is believed that the stability of these modes could depend very sensitively on very small differences in the pressure and q_ψ profiles. We do not understand why some discharges do, and others do not, exhibit coherent MHD activity, and a clear prescription for avoiding MHD activity in supershots has not been found.

The calculated q_ψ and total pressure profiles (including beam pressure) were used to study the ideal MHD stability of this supershot. The high-n stability was investigated using the EQGRUM [34] and STBAL [35] equilibrium codes. Figure 2 shows the profile of the gradient of the total pressure with respect to the normalized *poloidal* flux together with the boundary of the
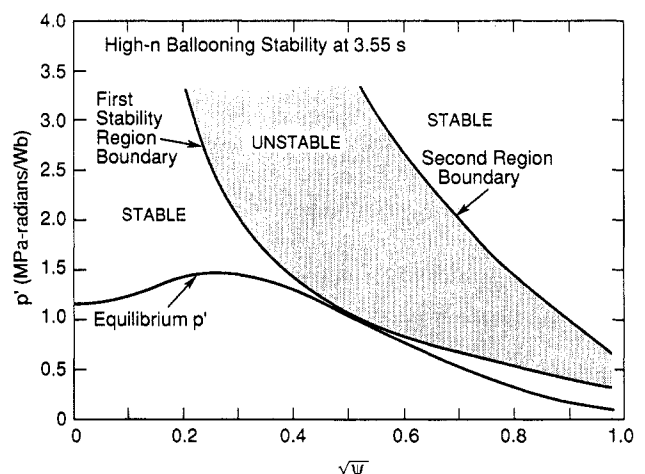

FIG. 2. Profile of the gradient of the total pressure with respect to the poloidal flux versus the square root of the normalized poloidal flux, compared with the boundary of the high-n ballooning unstable region.

TABLE II. FUSION PRODUCT PARAMETERS
COMPUTED FOR THE DD REACTIONS IN 55851

Fusion product	^{3}He	T
$n_{fp}(0)/n_e(0)$	2.2×10^{-5}	5.0×10^{-5}
$\beta_{fp}(0)$	6.8×10^{-6}	2.4×10^{-5}
$\langle \beta_{fp} \rangle$	8.6×10^{-7}	3.0×10^{-6}
$v_{fp}^{Birth}/v_{Alfvén}(0)$	0.90	1.05

unstable region. Both are plotted versus the square root of the normalized *poloidal* flux Ψ. This variable is roughly equal in magnitude to the x variable. The profiles are calculated to be stable to Mercier modes and marginally stable to high-n ballooning modes near x=0.5.

The low-n stability was analysed using the PEST 2 code [36]. The plasma was found to be marginally stable to an n=1 free boundary (conducting wall at infinity) kink/ballooning mode. The marginal stability value of β_{norm} is computed to be in the range 2.30–2.38, which is just above the actual value for the discharge (2.25). If the pressure is raised such that β_{norm} exceeds this value, the n=1 external kink/ballooning mode is predicted to be unstable.

4. TRANSP SIMULATION OF FUSION PRODUCTS FROM SUPERSHOT 55851

Various parameters for the T and ^{3}He fusion products (fp) from the DD reactions were computed using the Monte Carlo orbit model described in Section 1. The peak central densities of the unthermalized fp, as a fraction of the electron density during NBI, are listed in Table II. The fraction increases to higher values after termination of NBI since the thermal particle confinement time is short compared with the fp slowing down time and, thus, $n_e(0)$ decreases faster than $n_{fp}(0)$.

Another parameter of interest is the contribution of the fp pressure or β_{fp} to the total pressure or total toroidal β. Results are summarized in Table II. Still another parameter of interest is the ratio of the birth velocity v_{fp}^{Birth} of the fusion products to the central Alfvén velocity $v_{Alfvén}(0)$. The birth velocity is 7×10^6 m/s for ^{3}He and 8×10^6 m/s for T. The Alfvén velocity is given by

$$v_{Alfvén} = \frac{B_{TF}}{\sqrt{4\pi m_H(2n_D + n_H + 2n_{beam} + 15n_{imp})}} \quad (4)$$

where the average atomic mass of the impurities is approximated by 15 and the very small contribution from the fusion products is neglected. The peak central values of the ratio are also given in Table II. They are of interest for the TAE instability, which is discussed in Section 8.

The slowing down time and the average energy of the ^{3}He ions are also calculated. The average energy of the ^{3}He ions decreases from the birth energy of 0.8 MeV to 0.4 MeV late in the NBI phase. The slowing down time also decreases from 0.5 to 0.2 s during NBI.

5. GENERAL RESULTS FROM THE EQUIVALENT SIMULATIONS

The DT equivalent for each DD discharge in Table I was calculated using minimal changes in the TRANSP inputs for the DD modelling. The assumptions used for the modelling of the DD discharges differed, however, depending on available measurements. One major difference was the availability of T_i profile measurements. For the discharges that did not have measured profiles, the assumption $\chi_i = 2\chi_e$ was used to calculate T_i. This assumption adds uncertainty to the results for these discharges and makes comparisons between discharges more difficult.

The plasma densities are calculated in TRANSP using the particle balance equations. The electron density is symmetrized from the measured profile, so conservation of electrons determines the local radial flux of electrons. The values of Z_{eff} and the conservation of the impurity ion species determine the radial flux of the impurity. The D and T sources are determined by the NBI deposition profiles and by the D and T recycling. To solve the conservation equations for D and T, the relative fractions of the total numbers N_D and N_T in the initial (pre-NBI) plasma at the start of the calculation must be specified, and the relative radial fluxes of D and T must also be specified. Two specifications for the relative radial fluxes were investigated. For the cases listed in Table I, the radial velocities of D and T were assumed to be equal. An alternative choice, where the D and T diffusivities are assumed to be equal, gives similar results.

For simplicity, the only differences in the inputs for the DT equivalent simulations were (1) the change in the hydrogenic fractions of the initial (pre-NBI) plasma from typically 95% D and 5% H to 50% D and 50% T; (2) the change in recycling from 95% D^0 and 5% H^0 to 50% D^0 and 50% T^0; and (3) the

duplication of the NBI D^0 sources as T^0 sources, with the original powers split equally between the D^0 and T^0 sources. This procedure preserves the co/counter split of NBI.

The total hydrogenic recycling rates were not changed from those of the DD discharges, so assumption (2) means that the rates of D and T recycling are each half of the rate measured for the DD discharges. This models the case where the limiter would be saturated equally with both D and T. For the DT run scenarios planned for TFTR, the limiter is *not* expected to be saturated with T, so the hydrogenic recycling will be mainly D. Also T gas puffing is not planned, so the pre-NBI target plasmas for DT supershots are expected to be mainly C with some D.

Simulations of DT discharges with the alternative assumptions of relatively little T in the target plasma and in the recycling have been performed. The results for supershots are that the neutron yield and α parameters are insensitive to the assumptions (1) and (2). This is because most of the fuelling of the central region is from NBI. The beam deposition profiles of D and T NBI are similar, and the resulting central densities are predicted to be approximately equal. The total neutron emission rate depends mainly on the central D and T densities, but does not depend sensitively on the precise matching of the central D and T densities. In DT supershots, the density of T in the plasma edge is expected to be lower than that of D because of the reduced T recycling.

The values of Q for each DT/DD pair were calculated by dividing the peak fusion power yields by the injected NBI power. The total fusion power (thermonuclear + beam–target + beam–beam) was used. The calculated neutron rates were converted to fusion power using 17.6 MeV/neutron for DT and 7.3 MeV/neutron for DD. No reductions of the input power, such as those due to beam ion orbit loss or beam shine-through are included. The resulting Q values and their ratios are listed in Table I. Most of the calculated values for Q_{DD} agree with the experimental values to within the uncertainties of the neutron emission measurements. Both the measurements and the calculations normalize with the same NBI powers, so the uncertainty in the power does not enter in the uncertainty in Q_{DD}.

The *predicted* ratios Q_{DT}/Q_{DD}, given in Table I, are of interest for indicating the scaling from DD yields to DT yields. Some of the systematic errors in the predictions cancel in this ratio, so that it is more reliably predicted than either Q_{DD} or Q_{DT} separately. The predicted ratios for most of the
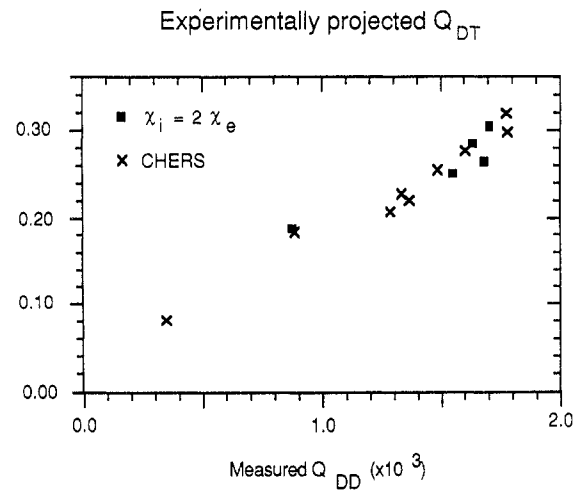
Experimentally projected Q_{DT}

FIG. 3. *Projected Q_{DT} calculated from the predicted ratio Q_{DT}/Q_{DD} times the measured Q_{DD} versus the measured Q_{DD} for the DD/DT equivalent pairs in Table I.*

supershots in Table I lie between 150 and 170. Most of the variation in the ratio comes from variation in T_i for the discharges. The Q_{DT}/Q_{DD} ratio decreases with T_i since Q_{DD} increases more rapidly with T_i than does Q_{DT}.

Independent calculations of Q_{DD} and Q_{DT} for the discharges in Table I were made with the SURVEY code. This is a steady state, fixed profile simulation code which uses the plasma parameters in the TRANSP analysis. It does not include any drift orbit effects (i.e. orbit spreading and orbit losses) in the modelling of fast ions or fusion products. The SURVEY results agree with the values from TRANSP to $\pm 5\%$. SURVEY was also used to determine the effects of two minor improvements that are not yet incorporated in most of the TRANSP simulations in Table I: (1) using the more accurate fusion cross-section fits of Bosch and Hale [29] instead of those of Duane [28], and (2) using the full-energy and half-energy fractions expected for T NBI instead of the D fractions. The net effect of the corrections on the ratio Q_{DT}/Q_{DD} is an increase of $(5 \pm 5)\%$ compared with the TRANSP values. The SURVEY result for the experimentally projected Q_{DT}, defined as the product of the calculated Q_{DT}/Q_{DD} times the measured Q_{DD}, is plotted versus the measured Q_{DD} in Fig. 3.

Predictions of neutron yields for DT experiments in JET have been published in Refs [12, 13]. The simulations in these papers are not DT equivalents of DD discharges since the beam voltages were increased (to 140 keV for D NBI and 160 keV for T NBI). Also
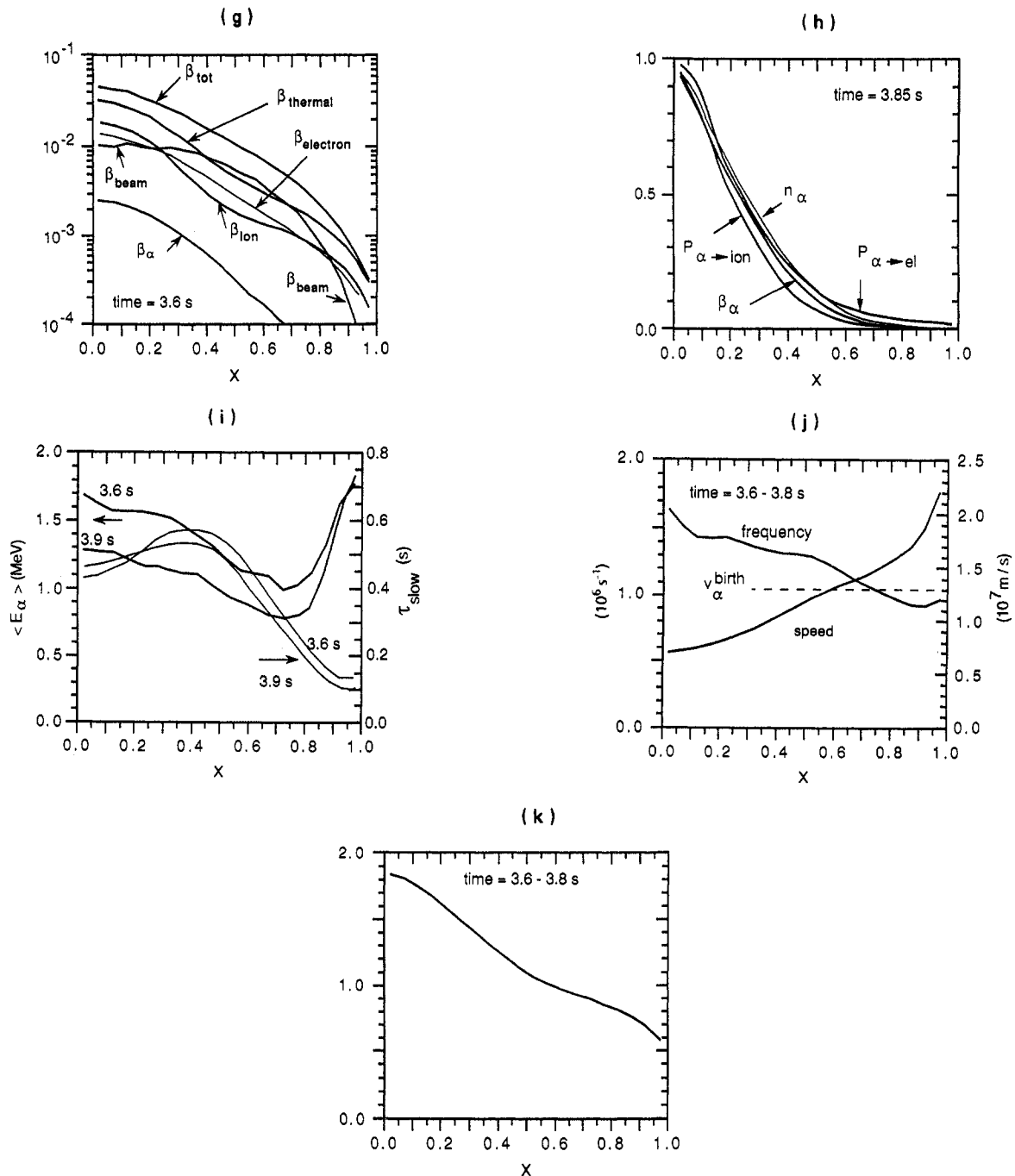
(a)

(b)

(c)

(d)

(e)

(f)
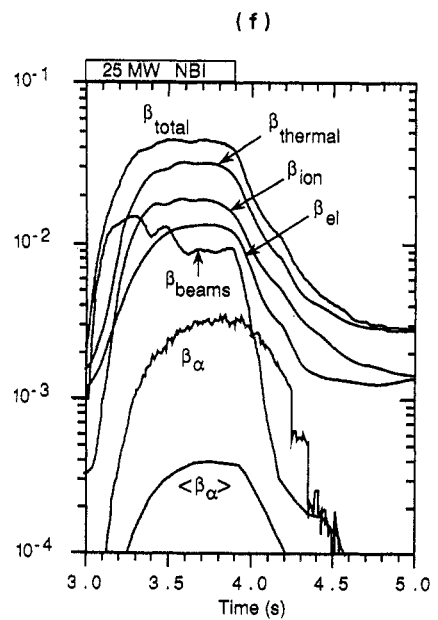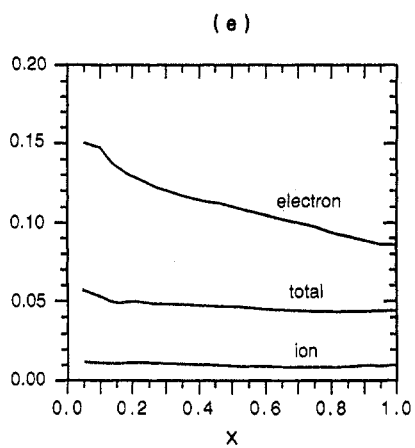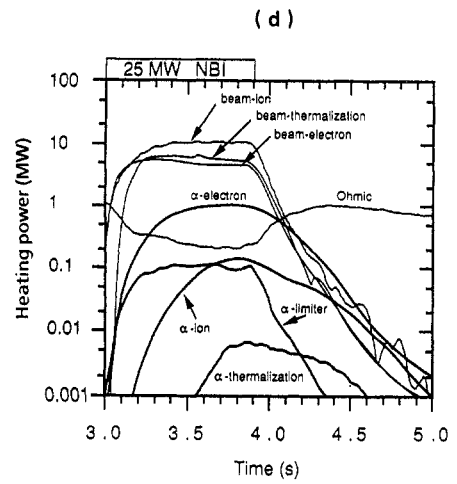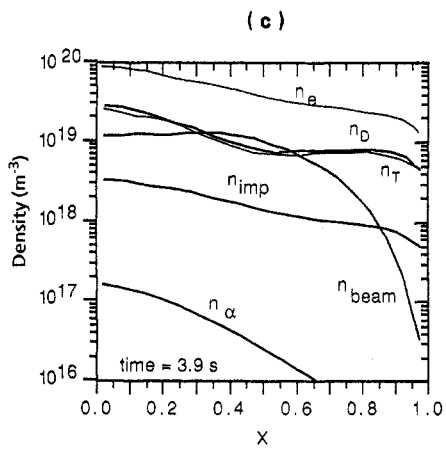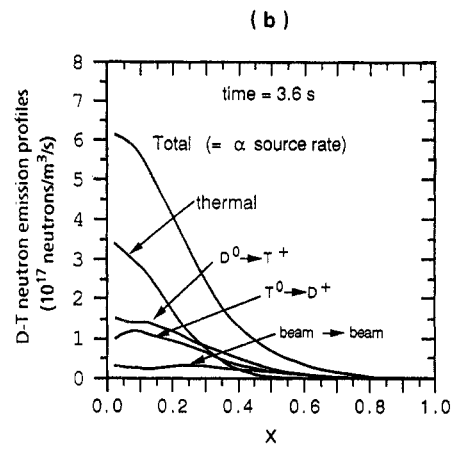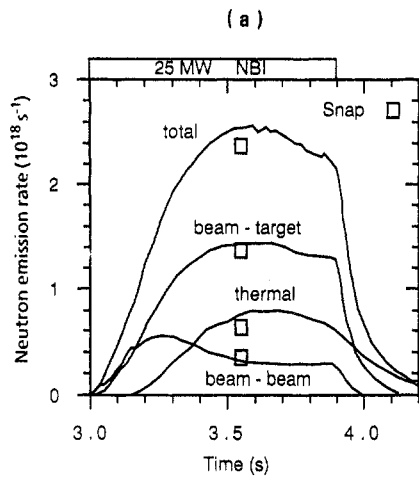
FIG. 4. Results from the DT equivalent simulation based on supershot 55851.

(a) DT fusion reaction rates versus time.

(b) Profile of the DT neutron emissivities.

(c) Measured profile of n_e, and computed profiles of n_{beam}, n_D, n_T, n_{imp} and n_α at the end of NBI.

(d) Volume integrated heating powers versus time.

(e) Ratio of the volume integrated α heating power to the volume integrated power loss rate for the thermal ions and electrons, and for both, at the end of NBI.

(f) Components of $\beta(0)$ and $\langle\beta_\alpha\rangle$ versus time. The effects of post-NBI sawteeth can be seen in $\beta_\alpha(0)$.

(g) Profiles of the components of β_{tor}.

(h) Profiles of the α production, density, heating and β_α normalized to 1 at x = 0.

(i) Profiles of the α slowing down time and the average α energy.

(j) Profiles of the Alfvén frequency and the Alfvén speed. The speed of the initial α particles is indicated.

(k) Profile of the ratio of the α birth speed and the Alfvén speed.

the definition of Q in these papers is not the same
as the one used here, since the absorbed beam power
minus the rate of increase of the total energy (dW/dt)
is used instead of the full NBI power for the thermo-
nuclear contribution to the total neutron yield. The
predictions for Q_{DT} using the JET definitions are in the
range 0.72–0.76. If these corrections for NBI power
are not included, as is the case for the TFTR values
predicted here, the Q_{DT} values are estimated to be
0.51–0.54.

Results for the peak values of $\beta_\alpha(0)$ and $\langle\beta_\alpha\rangle$ are
also shown in Table I. Peak values for the ratio
$n_\alpha(0)/n_e(0)$ during the NBI phase of the discharges
are close to the values of $\langle\beta_\alpha\rangle$ (typically within 15%).

6. FUSION YIELDS AND α PARAMETERS
FROM THE DT EQUIVALENT SIMULATION
OF SUPERSHOT 55851

Results from the DT equivalent simulation of super-
shot 55851 are summarized in Figure 4. The neutron
rates are shown in Fig. 4(a). The peak beam–target
contribution is 55% of the total, as in the DD result
(Fig. 1(h)), and the peak thermonuclear contribution
is 30% of the total. The total DT neutron rate is the
α source rate. Profiles of the components of the DT
fusion emission are shown in Fig. 4(b). Besides the
DT reaction (Eq. (1c)), TRANSP computes the DD
fusions (Eqs (1a, b)) and TT fusions with much lower
rates. The total rate gives $Q_{DT} = 0.28$, which is close
to the highest values shown in Table I.

Profiles of densities at the end of NBI are shown
in Fig. 4(c). The fast α density is much more peaked
and much lower than the electron density. The central
value is 0.3% of that of the electron density and more
than an order of magnitude below the impurity density.
After NBI, the decrease in the α density is not as rapid
as the decrease in the electron density, since the α
slowing down time is long relative to the thermal
particle confinement time.

The volume integrated heating powers are shown in
Fig. 4(d). Most of the α heating is to the electrons,
$P_{\alpha-e}$. This is overshadowed by the NBI heating during
the NBI phase and by the Ohmic heating after NBI.
The α heating of ions, $P_{\alpha-ion}$, is lower than $P_{\alpha-e}$
by nearly an order of magnitude. The predicted orbit
loss of α particle power to the limiter and walls is
less than 10% of the total α heating rate.

The proximity to central ignition [3] can be indi-
cated by the ratios of the α heating and power loss
terms:

$$\frac{\displaystyle\int_0^x P_{\alpha-j}\,dV}{\displaystyle\int_0^x P_{j-loss}\,dV} \tag{5}$$

with j = either the thermal ions, the electrons, or both
(the total thermal plasma). The loss channel for elec-
trons is convection, conduction and radiation, and that
for ions is convection, conduction and net charge
exchange. The ion–electron coupling would add to the
ion loss and subtract from the electron loss, cancelling
for the total thermal plasma. These ratios are shown
in Fig. 4(e). Central ignition would occur if the ratio
for the thermal plasma were more than 1 in the
vicinity of x = 0. The ignition margin, defined as
the ratio for the total thermal plasma at x = 1, is
predicted to be 4%.

The central values of the various contributions to the
toroidal β are shown in Fig. 4(f). The volume averaged
values of β_α are also shown. The peak value, $\beta_\alpha(0) =$
0.3%, is within the range projected in Refs [1, 2 and 4]
(0.16–0.50%) and is comparable to the highest values
given in Table I. Profiles of the contributions to the
toroidal β near the time of peak β are shown in
Fig. 4(g). Relative profiles for the α density, β_α, and
heating rates near the end of NBI are shown in
Fig. 4(h). These profile shapes are very similar to
each other, except that the α heating of electrons is
slightly broader and the α heating of ions is slightly
narrower than the others.

Profiles of the slowing down time and the average
energy of the α particles are shown in Fig. 4(i). The
value of the central slowing down time is $\tau_{slow}(0) \approx$
0.4 s between 3.6 s and 3.9 s. The average energy in
the central region drops slowly, reaching an approxi-
mately steady state value by the end of NBI. The
energy distribution function is thus not in steady state
at early times or even at the time of peak neutron
production.

The Alfvén velocity for the DT simulations is
given by

$$v_{Alfvén} = \frac{B_{TF}}{\sqrt{4\pi m_H(2n_D+3n_T+2.5n_{beam}+4n_\alpha+15n_{imp})}} \tag{6}$$

The values given by this expression differ slightly from
the values given by Eq. (4) for the DD reaction because
of the different masses of the ions. The profile of the
flux surface average of this velocity is shown in
Fig. 4(j); also shown is the profile of the flux surface
average of the Alfvén frequency, estimated [37, 38] by

$$\omega_{Alfv\acute{e}n} \approx \frac{V_{Alfv\acute{e}n}}{2q_\psi R} \tag{7}$$

The ratio of the α birth velocity $(1.3 \times 10^7$ m/s) to the flux averaged Alfvén velocity is shown in Fig. 4(k). Implications of these parameters are discussed in Section 8.

The results from this particular equivalent simulation are fairly representative of the results from the best supershots listed in Table I.

7. DT EXTRAPOLATIONS

There are reasons to suspect that the actual DT plasma performance in TFTR might be better than that indicated by the equivalent simulations. We describe a DT extrapolation in order to provide an example of neutron yields and α parameters which potentially will occur, and also to indicate what improvements would be required to enhance the yield and the α parameters. A DT plasma with the same setup and NBI parameters as supershot 55851 could be expected to perform better than the DD plasma because of the potentially favourable mass scaling of confinement and the α heating of electrons. The equivalent simulations use the actual measured profiles, so the advantage of these possibilities is not claimed for them.

The NBI power for supershot 55851 was relatively low (25 MW) compared to the highest NBI power achieved in TFTR (33 MW). If MHD and Z_{eff} can be controlled, then, as the power increases, the plasma density and energy increase, giving a higher neutron yield and increased α parameters. Despite this, the higher power supershots listed in Table I did not have substantially better Q_{DT} yields. However, with the accumulation of more operating experience, better performance may be expected.

The extrapolations were derived by scaling the parameters of discharge 55851 to higher power using empirical scaling relations which have been derived from a statistical analysis of more than 550 TFTR supershots from 1990 [39]. These scaling relations give the central plasma parameters at the time of maximum neutron emission, $n_e(0)$, $n_D(0)$, $T_e(0)$ and $T_D(0)$, as single products of powers of B_{TF}, P_{NBI}, I_p, E_{NBI} and τ_E^{total}. E_{NBI} is the energy of the full-energy component of the NBI. The total energy confinement time τ_E^{total} is given as a product of powers of B_{TF}, C_{target}, I_p, $(1 + F_{NBI})$ and E_{NBI}, where C_{target} is the average C II emission in the target plasma just

before NBI, and F_{NBI} is the fraction of the NBI power in the co-direction.

Not all the parameters for discharge 55851 were predicted well by the empirical scaling relations; this is probably due to the lithium pellet injection and the current ramp. The values of $n_e(0)$ and $n_D(0)$ were 40% higher than the values given by the empirical scaling relations, whereas the values of $T_e(0)$, $T_D(0)$, τ_E^{total} and the peak neutron rate were consistent. A DD extrapolation of discharge 55851 was derived by increasing P_{NBI}, I_p and C_{target}, using the scaling relations to give multipliers of $n_e(0)$, $n_D(0)$, $T_e(0)$, $T_D(0)$ and τ_E^{total}. This scaled DD supershot was converted to a DT supershot, incorporating some of the anticipated α heating of electrons.

The NBI power was increased from 25 to 35 MW, and the plasma current was increased by a factor of 1.2 to a peak value of 1.95 MA, which is close to the present empirical upper limit for achieving supershots in TFTR. The scaling variation with I_p is not favourable, but I_p was increased in order to keep β_{norm} from surpassing the present empirical limit for supershots (around 2.7). B_{TF} was held constant, although the scaling relations predict a rapid improvement of plasma performance with increasing B_{TF}. F_{NBI} and E_{NBI} were kept near their values for discharge 55851 (approximately 0.57 keV and 105 keV), even though the scaling relations favour a *decrease* of E_{NBI}.

With P_{NBI}, I_p, B_{TF}, E_{NBI} and F_{NBI}, as chosen above, the scaling of $n_e(0)$, $n_D(0)$, $T_e(0)$ and $T_D(0)$ is determined solely by τ_E^{total}, which decreases weakly with increasing C_{target}. We assumed that τ_E^{total} would remain at the value observed for discharge 55851 (0.17 s). The scaling relations require that C_{target} would increase by 15%. An increase of C_{target} with increased NBI power would be expected because of the increased power loading on the limiter. With these choices of parameters, the scaling relations imply that $n_e(0)$ and $n_D(0)$ would increase by 15%. The latter two quantities determine Z_{eff}, which would be slightly below the values observed in discharge 55851. The scaling of $T_D(0)$ results in a 7% increase and that of $T_e(0)$ results in a 4% increase.

To convert the DD extrapolation to a DT extrapolation, we assume, as in the equivalent simulations, that n_D is replaced by a 50/50 mix of n_D and n_T in the pre-NBI target, and that the NBI used equal amounts of D and T. $T_e(0)$ could be expected to be higher than indicated by the DD scaling relations owing to the α heating and possibly the favourable isotope scaling. In order to incorporate the α heating, we consider the ratio
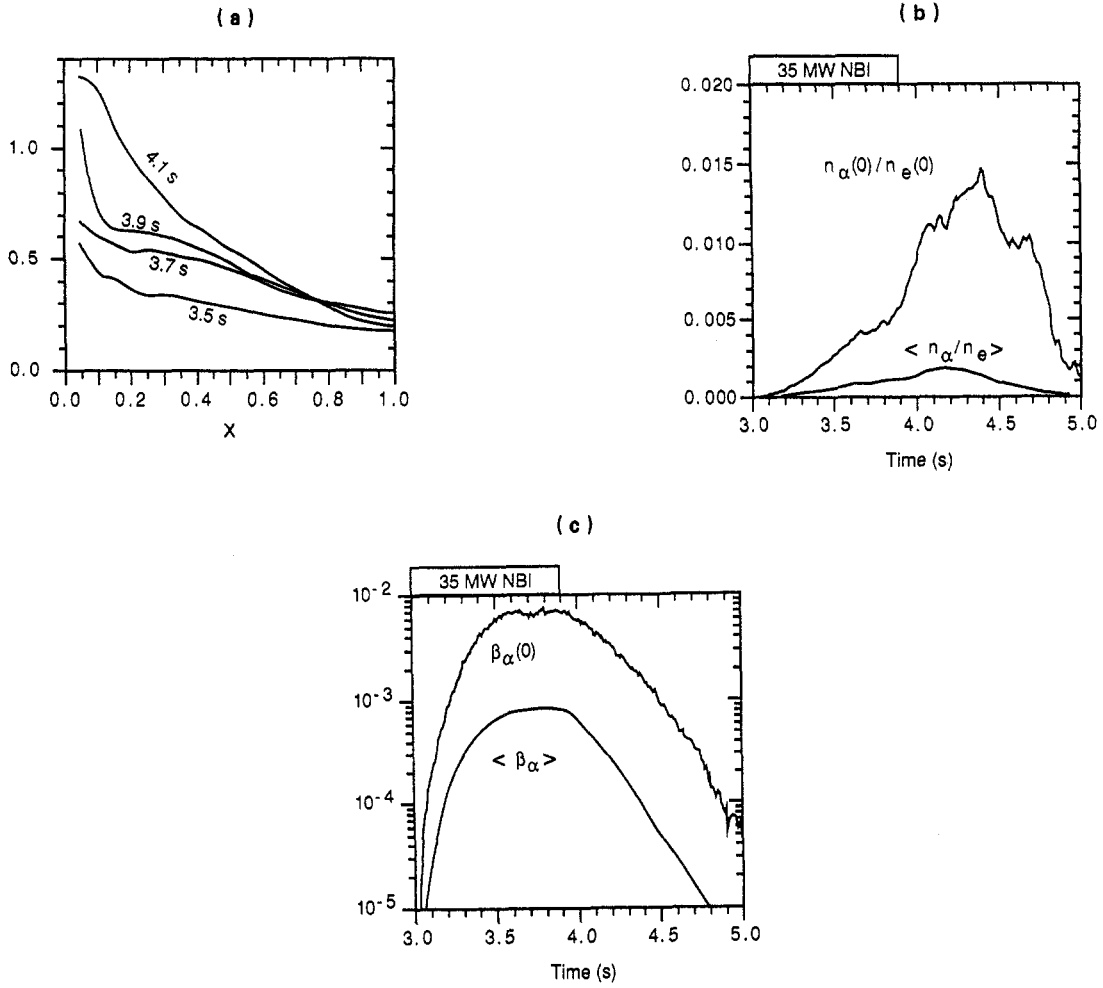
(a)

(b)

(c)

FIG. 5. *TRANSP results for the DT extrapolation.*

(a) Profile of the ratio of the volume integral of the α heating of electrons and the beam–electron and ion–electron coupling.

(b) Ratio of the central densities of α particles and electrons.

(c) Central and volume averaged β_α. Sawteeth were not modelled.

$$\frac{\displaystyle\int_0^x P_{\alpha\to e}\, dV}{\displaystyle\int_0^x [P_{beam\to e} + Q_{ie}]\, dV}$$

where Q_{ie} is the ion → electron heat coupling. This ratio obtains high values outside $x = 0.25$ (the half-radius of the neutron emission profile), as shown in Fig. 5(a). Even at $x = 1$, the ratio is 0.24. This increased heating could result in an increase in T_e, or a loss in energy confinement (increase in χ_e), or both.

To compromise, we assume that T_e will increase by 21% more than the amount given by the DD

scaling of discharge 55851, i. e. by a total of 25%. These resulting scaling factors were used as multiplicative factors on the whole, time dependent profiles from discharge 55851, and the resulting profiles were modelled with TRANSP.

The results from the DT extrapolation simulation and comparisons with the DT equivalent simulation are summarized in Table III. The increase of T_e increases the total energy, resulting in τ_E^{total} being higher than would be given by the DD scaling relations. Plots of the results are shown in Fig. 5. The peak beam–target contribution is 57% of the total and the peak thermonuclear contribution is 24% of the total. The profiles of the α effects from the extrapolation are quite similar

TABLE III. SUMMARY OF PARAMETERS
AND RESULTS FROM THE DT EQUIVALENT
SIMULATION OF SUPERSHOT 55851 AND
FROM THE DT EXTRAPOLATION BASED ON
EMPIRICAL SCALING RELATIONS AND
IMPROVED STABILITY LIMITS

	DT equivalent	DT extrapolation
P_{NBI} (MW)	24.6	35
I_p (MA)	1.58	1.95
$n_e(0)$ (10^{20} m^{-3})	0.95	1.07
$T_e(0)$ (keV)	10.2	12.8
$T_i(0)$ (keV)	22.5	24.0
Z_{eff}	2.8	2.3
β_{norm}	2.25	2.8
Q_{DT}	0.28	0.37
$\beta_\alpha(0)$ (%)	0.28	0.7
$\langle \beta_\alpha \rangle$ (%)	0.04	0.09
$n_\alpha(0)/n_e(0)$ (%)	0.2	0.6
$\tau_E^{thermal}$ (s)	0.13	0.10
τ_E^{total} (s)	0.17	0.19
$\int P_{\alpha-e} dV$ (MW)	1.1	2.1
$v_\alpha^{Birth}/v_{Alfvén}$ (0)	1.85	2.0

to those of the equivalent simulation, but scaled up in magnitude. The ratio $n_\alpha(0)/n_e(0)$ increases to 15% after NBI, as shown in Fig. 5(b). Values for $\beta_\alpha(0)$ and $\langle \beta_\alpha \rangle$ are shown in Fig. 5(c). The result for the ratio of the integrated α heating power to the total thermal losses for the extrapolation, corresponding to the middle curve in Fig. 4(e), is that $\int P_{\alpha-th}/\int P_{loss}$ reaches 0.17 near the plasma centre.

Since these extrapolations would have to be MHD stable to be viable, the ideal MHD stability has been studied. PEST calculations indicate that the extrapolation discussed here is unstable to high-n modes in the central region. It is not known if minor modifications of the q_ψ and pressure profiles would lead to ideal MHD stability. This extrapolation suggests that the stability limits may need to be improved for TFTR to achieve higher α parameters.

Other scenarios for DT experiments which could increase the neutron yield and the α parameters have been proposed. They include: (1) establishing the

supershot with a purely T plasma using T NBI, and then abruptly switching to D NBI; (2) using T pellet injection to fuel a target plasma, and then using D NBI and ICRH to heat the plasma; and (3) compressing a supershot. Scenario (1) would transiently increase the neutron yield, but the NBI sources in TFTR cannot be switched from T to D fast enough. Scenario (2) allows comparable values of Q_{DT} and β_α to be achieved with much less tritium consumption per pulse. Simulations with scenario (3) yielded neutron rates and β_α values that were higher than those calculated for the DT equivalent simulations, but for short durations.

8. THEORETICAL ASPECTS OF α INSTABILITIES

There are two classes of collective α instabilities that may have serious consequences for α particle confinement: (1) the toroidicity induced Alfvén eigenmodes (TAE) [37, 40] and (2) the kinetic ballooning modes (KBM) [41]. They are similar in that both are discrete modes and in that they can be resonantly destabilized by circulating and trapped α particles when the α pressure is sufficiently steep and β_α is sufficiently large. The predicted frequencies of these modes are:

$$\omega_{TAE} \approx \tfrac{1}{2} \omega_{Alfvén} \tag{8a}$$

$$\omega_{KBM} \approx \omega_{*ip} \equiv -k_\theta \rho_i v_{ti} \frac{d \ln \rho_i}{dr} \tag{8b}$$

where ω_{*ip} is the ion diamagnetic drift frequency, ρ_i is the ion Larmor radius and v_{ti} is the ion thermal velocity. Figures 4(g) and 4(h) show that the region of steep pressure corresponds roughly to $x \equiv r/a < 0.4$.

The dominant contribution to instability comes from the most energetic class of α particles that can satisfy the resonance condition [38, 41]:

$$\omega \equiv \omega_d \pm p \omega_{b,t} \qquad p = 0, 1, 2, \ldots$$

where ω_d is the magnetic drift frequency and $\omega_{b,t}$ is the α bounce (transit) frequency. The frequently quoted criterion that the α particles must be super-Alfvénic for TAE modes, however, is not necessary for instability. Generally speaking, the lowest β_α threshold for these modes occurs when $v_\alpha^{Birth}/v_{Alfvén} \approx 1$, taking all other parameters to be fixed. Figure 4(k) shows that this condition occurs in the vicinity of $x \approx 0.6$, but this is not the region of steep α pressure gradient
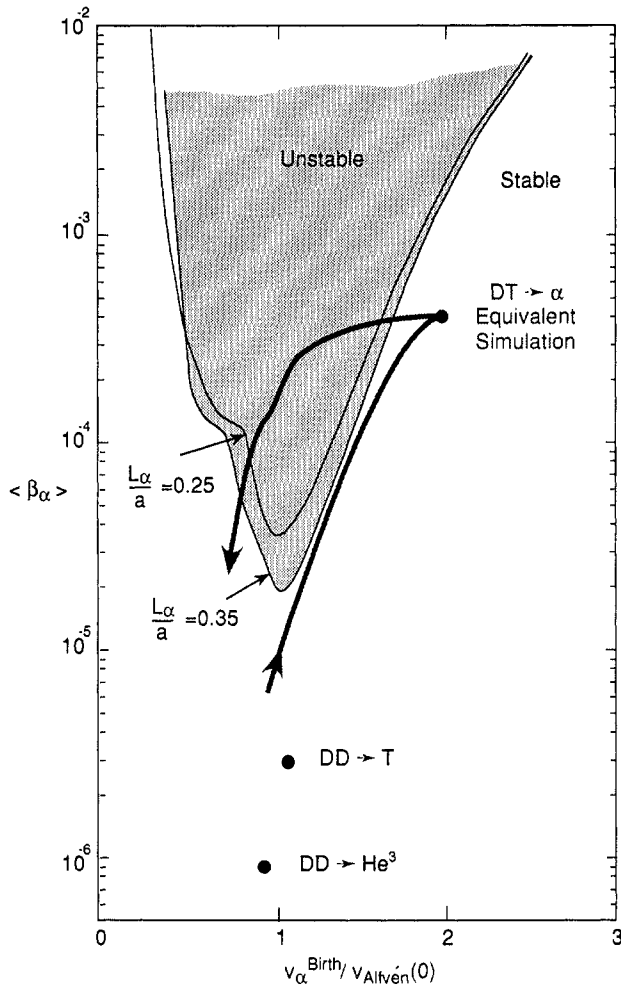
FIG. 6. Calculated boundary of the TAE instability region in the volume averaged $\beta_{fusion\ product}$ versus the central value of the ratio of the fusion product birth speed and the Alfvén speed. The $\beta_{fusion\ product}$ was assumed to decay exponentially in minor radius with a decay length of L_α/a = 0.25 or 0.35. The decay length in the DT equivalent simulation lies between these values. The trajectory of the DT → α equivalent simulation is shown, with the closed circle indicating the end of NBI. The locations of the DD → ^{3}He and DD → T predictions are also shown.

(Fig. 4(g)). The region x < 0.6 can still be unstable, but requires higher values of β_α [40].

A calculation was performed using the NOVA-K code of the threshold for the TAE instability [40]. The plasma parameters were those of supershot 55851 near 3.6 s. The boundary of the unstable region and the trajectory followed by the DT equivalent simulation are shown in Fig. 6. The trajectory passes close to the boundary around the time of maximum neutron emission as $\langle\beta_\alpha\rangle$ increases. The boundary of the unstable region changes as the plasma parameters change,

decreasing to lower values of $\langle\beta_\alpha\rangle$ as the density and pressure decrease. Thus, when $\langle\beta_\alpha\rangle$ is greater than 2×10^{-5}, mechanisms that would cause $v_{Alfvén}$ to increase without decreasing $\langle\beta_\alpha\rangle$ are predicted to plunge the discharge into the TAE unstable region. This circumstance happens naturally after NBI, and the trajectory is predicted to pass through the unstable region for 0.3 s, offering an opportunity to observe the TAE instability.

Mechanisms which decrease $\langle\beta_\alpha\rangle$ apparently would shift the trajectory below the unstable region. The post-NBI sawteeth occurring in discharge 55851 were modelled in the DT equivalent simulation and found to flatten the n_α profile briefly, but not to increase the global loss of α particles or to decrease $\langle\beta_\alpha\rangle$, as shown in Fig. 4(f). The trajectory shown in Fig. 6 is typical of the results from other DT equivalent simulations of supershots in Table I. The trajectories for the DD fusion products (see Table II) are also indicated in Fig. 6 and are far below the unstable region.

An important distinction between the TAE and the KBM instabilities is that the KBMs are excited only when the plasma is close to the first stability ballooning boundary, whereas TAE modes can exist even below this boundary. The *local* proximity to ideal ballooning marginality is the relevant criterion. Indeed, the plasma could be close to the ballooning limit in the regions of weak magnetic shear. For the DT equivalent simulation, it can be seen from Fig. 1(k) that in the region x < 0.3 the plasma is calculated to have low shear. The results in Fig. 2 confirm the conclusion that the discharge is close to the stability limit for the region 0.3 < x < 0.6. Since this region overlaps with the region of steep α pressure, destabilization of KBMs appears possible [41].The threshold value of β_α at which KBMs become destabilized requires a careful assessment of the importance of continuum damping for these modes, which awaits further work.

As for the TAE modes, an important question is to determine over what extent of the plasma an Alfvén continuum gap structure exists [40]. To leading order in inverse aspect ratio, the centre of the gap is roughly proportional to $\omega_{Alfvén}$, which is plotted in Fig. 4(j). To this order, it can be determined on the basis of Fig. 4(j) that a gap structure exists in the region x < 0.4 since $\omega_{Alfvén}$ is relatively flat here. However, inverse aspect ratio corrections will enhance the gap centre values, so that the gap structure may extend across the plasma to the edge [40]. This is the most unstable scenario, and theoretical understanding in this area is still evolving.

9. SUMMARY

The TRANSP code has been used to model pairs of DT/DD discharges in TFTR. The DD discharges are actual TFTR discharges, including supershots with the highest measured neutron rates and Q_{DD}. Detailed comparisons of predictions and measurements are shown for one supershot to indicate that accurate agreement with measurements is achieved. Corrections, such as for the $T_i - T_{imp}$ differences, have been included and found to change the calculated neutron rates by $\approx 5\%$. Fusion products from the DD reactions in this discharge have been calculated and, as expected, their parameters are very small.

The DT equivalent simulations are conservative, assuming minimal alterations of actual DD discharges. These calculations give the computed ratio Q_{DT}/Q_{DD} for supershots to be typically in the range 150–175, with the maximum calculated $Q_{DT} \approx 0.3$. The maximum α parameters are $\beta_\alpha(0) \approx 0.5\%$ and $n_\alpha(0)/n_e(0) \approx 0.35\%$. The α effects appear to be large enough that the TAE and the KBMs could be observed, particularly during the period of decreasing density after the end of NBI. The sawteeth often observed after NBI in supershots are predicted to not decrease $\langle \beta_\alpha \rangle$ and thus to not terminate the TAE instability.

A DT extrapolation of an MHD free supershot to full NBI parameters is derived from empirical supershot scaling relations. The value of Q_{DT} is calculated to increase from 0.28 at 25 MW NBI to 0.37 at 35 MW NBI. The MHD stability of this extrapolation is, however, problematic.

Appendix

The impurity temperature $T_{imp} \equiv T_x$ is calculated in TRANSP, using the local heating power density delivered to impurities (including beam heating, radiofrequency heating, compressional heating, viscous heating and fast ion heating from fusion products), power flows due to particle convection and a local model of conductive losses.

The equations that describe the time evolution of impurity energy density and hydrogenic energy density are:

$$\frac{\partial}{\partial t} (\tfrac{3}{2} n_x T_x) = q_x - c \nabla \cdot (\Gamma_x T_x) + \frac{\tfrac{3}{2} n_x (T_i - T_x)}{\tau_{xi}}$$

$$+ \frac{\tfrac{3}{2} n_x (T_e - T_x)}{\tau_{xe}} - \frac{\tfrac{3}{2} n_x T_x}{\tau_E^{ion}} \quad \text{(A.1)}$$

$$\frac{\partial}{\partial t} (\tfrac{3}{2} n_i T_i) = q_i + q_{bth} - c \nabla \cdot (\Gamma_i T_i) + \frac{\tfrac{3}{2} n_i (T_x - T_i)}{\tau_{ix}}$$

$$+ \frac{\tfrac{3}{2} n_i (T_e - T_i)}{\tau_{ie}} - \frac{\tfrac{3}{2} n_i T_i}{\tau_E^{ion}} \quad \text{(A.2)}$$

where the subscripts x and i indicate impurity ions and main ions, respectively, q_x and q_i are the collisional beam power coupling to the impurity and thermal ions, and q_{bth} is the beam thermalization power ($\tfrac{3}{2} S_b^{th} T_i$). Γ is the particle flux, derived from the continuity equation for each species, c is the convective multiplier (typically specified as $\tfrac{3}{2}$ by the user), τ_{xi} is the temperature relaxation time for impurities on the main ions, τ_{ix} is the temperature relaxation time for the main ions on impurity ions, τ_{xe} is the temperature relaxation time of impurities on electrons, τ_{ie} is the temperature relaxation time of main ions on electrons, and τ_E^{ion} is a local ion energy confinement time whose value will be determined self-consistently.

To determine the proper expression for τ_E^{ion} which makes Eqs (A.1) and (A.2) a self-consistent local model of the ion energy balance, we will sum the equations, making use of the following identities and definitions:

$$0 = \frac{\tfrac{3}{2} n_x (T_x - T_i)}{\tau_{xi}} + \frac{\tfrac{3}{2} n_i (T_i - T_x)}{\tau_{ix}}$$

$$q_{ei} \equiv \frac{\tfrac{3}{2} n_x (T_e - T_x)}{\tau_{xe}} + \frac{\tfrac{3}{2} n_i (T_e - T_i)}{\tau_{ie}}$$

$$q_h \equiv q_i + q_x + q_{bth} \quad \text{(A.3)}$$

$$q_{conv} \equiv c \nabla \cdot (\Gamma_x T_x + \Gamma_i T_i)$$

$$W_i \equiv \tfrac{3}{2} (n_i T_i + n_x T_x)$$

where q_{ei} represents the total power density transfer from electrons to all thermal ions (hydrogenic + impurity), q_h is the total heating power density to the thermal ions, q_{conv} is the total convective power flow and W_i is the total thermal ion energy density. The sum of Eqs (A.1) and (A.2) becomes

$$\frac{\partial W_i}{\partial t} = q_h + q_{ei} - q_{conv} - \frac{W_i}{\tau_E^{ion}} \quad \text{(A.4)}$$

Since all of the terms in this equation are available to TRANSP except τ_E^{ion}, we can solve for it:

$$\tau_E^{ion} = \frac{W_i}{q_h + q_{ei} - q_{conv} - \dfrac{\partial W_i}{\partial t}} \tag{A.5}$$

For each transport time step, TRANSP advances Eq. (A.1) in time, using the τ_E^{ion} determined from Eq. (A.5).

ACKNOWLEDGEMENTS

REFERENCES

[1]   JASSBY, D.L., BARNES, C.W., BELL, M.G., et al., Phys. Fluids B **3** (1991) 2308; and references therein.

[2]   MEADE, D.M., ARUNASALAM, V., BARNES, C.W., et al., in Plasma Physics and Controlled Nuclear Fusion Research 1990 (Proc. 13th Int. Conf. Washington, DC, 1990), Vol. 1, IAEA, Vienna (1991) 9.

[3]   REDI, M., ZWEBEN, S., BATEMAN, G., Fusion Technol. **13** (1988) 57.

[4]   ZWEBEN, S.J., FURTH, H.P., MIKKELSEN, D.R., et al., Nucl. Fusion **28** (1988) 2230.

[5]   STRACHAN, J.D., ZWEBEN, S.J., BARNES, C.W., et al., in Plasma Physics and Controlled Nuclear Fusion Research 1988 (Proc. 12th Int. Conf. Nice, 1988), Vol. 1, IAEA, Vienna (1989) 257.

[6]   GOLDSTON, R.J., in Basic Physical Processes of Toroidal Fusion Plasmas (Proc. Course and Workshop Varenna, 1985), Vol. 1, Monotypia Franchi, Perugia (1986) 165.

[7]   HAWRYLUK, R.J., in Physics of Plasma Close to Thermonuclear Conditions (Proc. Course Varenna, 1979), Vol. 1, CEC, Brussels (1980) 19.

[8]   ZARNSTORFF, M.C., McGUIRE, K., BELL, M.G., et al., Phys. Fluids B **2** (1990) 1852.

[9]   STRACHAN, J.D., BITTER, M., RAMSEY, A.T., et al., Phys. Rev. Lett. **58** (1987) 1004.

[10]   KADOMTSEV, B.B., Sov. J. Plasma Phys. **1** (1975) 389.

[11]   MERCIER, C., LUC, H., in Instabilities and Confinement in Toroidal Plasmas (Proc. Course Varenna, 1971), CEC, Luxembourg (1974) 63.

[12]   JET Team, Plasma Phys. Control. Fusion **32** (1990) 1083.

[13]   BALET, B., CORDEY, J.G., STUBBERFIELD, P.M., Plasma Phys. Control. Fusion **32** (1990) 106.

[14]   SNIPES, J.A., TERRY, J.L., MARMAR, E.S., et al., in Controlled Fusion and Plasma Physics (Proc. 18th Eur.

[15]   TAYLOR, G., EFTHIMION, P., McCARTHY, M., et al., Rev. Sci. Instrum. **55** (1984) 1739.

[16]   CAVALLO, A., CUTLER, R.C., McCARTHY, M.P., Rev. Sci. Instrum. **59** (1988) 899.

[17]   STAUFFER, F.J., BOYD, D.A., CUTLER, R.C., et al., Sci. Instrum. **59** (1988) 2139.

[18]   JOHNSON, D., BRETZ, N., GREK, B., LONG, D., PALLADINO, R., TOLNAS, E., Rev. Sci. Instrum. **57** (1986) 1856.

[19]   STRATTON, B., FONCK, R.J., JAEHNIG, K.P., et al., in Time Resolved Two- and Three-Dimensional Plasma Diagnostics (Proc. Tech. Comm. Mtg Nagoya, 1990), IAEA, Vienna (1991) 78.

[20]   HSUAN. H., BITTER, M., RICE, J.E., et al., Rev. Sci. Instrum. **59** (1988) 2127.

[21]   PARK, H., Plasma Phys. Control. Fusion **31** (1989) 2035.

[22]   ZARNSTORFF, M., BELL, M.G., BITTER, M., et al., Phys. Rev. Lett. **60** (1988) 1306.

[23]   FONCK, R.J., RAMSEY, A.T., YELLE, R.V., Appl. Opt. **21** (1982) 2115.

[24]   HILL, K.W., BITTER, M., BRETZ, N.L., et al., Nucl. Fusion **26** (1986) 1131.

[25]   BUDNY, R., and TFTR Group, J. Nucl. Mater. **176&177** (1990) 427.

[26]   HENDEL, H., PALLADINO, R.W., BARNES, C.W., et al., Rev. Sci. Instrum. **61** (1990) 1900.

[27]   TOWNER, H.H., GOLDSTON, R., Bull. Am. Phys. Soc. **29** (1984) 1305.

[28]   DUANE, B.H., Fusion Cross Section Theory, Annual Report on CTR Technology 1972, BNWL-1685, Battelle Pacific Northwest Laboratory, Richland, WA (1972).

[29]   BOSCH, H.-S., HALE, G.M., Improved Formulas for Fusion Cross Sections and Thermal Reactions, Rep. IPP 1/252, Max-Planck-Institut für Plasmaphysik, Garching (1990); to be published in Nucl. Fusion.

[30]   ROQUEMORE, A.L., CHOUINARD, R.C., DIESSO, M., PALLADINO, R., STRACHAN, J.D., TAIT, G.D., Rev. Sci. Instrum. **61** (1990) 3163.

[31]   HILL, K.W., VON GOELER, S., BITTER, M., et al., Rev. Sci. Instrum. **56** (1985) 830.

[32]   JOHNSON, L.C., BITTER, M., CHOUINARD, R., YOUNG, K.M., Rev. Sci. Instrum. **57** (1986) 2133.

[33]   MANICKAM, J., ARUNASALAM, V., BARNES, C.W., et al., in Plasma Physics and Controlled Nuclear Fusion Research 1988 (Proc. 12th Int. Conf. Nice, 1988), Vol. 1, IAEA, Vienna (1989) 395.

[34]   DELUCIA, J., JARDIN, S.C., TODD, A.M.M., J. Comput. Phys. **37** (1980) 183.

[35]   PHILLIPS, M.W., TODD, A.M.M., HUGHES, M.H., MANICKAM, J., JOHNSON, J.L., PARKER, R.R., Nucl. Fusion **28** (1988) 1499.

[36]   GRIMM, R.C., DEWER, R.L., MANICKAM, J., J. Comput. Phys. **49** (1983) 94.

[37]   CHEN, L., in Theory of Fusion Plasmas (Proc. Joint Varenna–Lausanne Int. Workshop Chexbres, 1988), Editrice Compositori, Bologna (1989) 327.

[38]   BIGLARI, H., ZONCA, F., CHEN, L., On Resonant Destabilization of Toroidal Alfvén Eigenmodes by

Conf. Berlin, 1991), Vol. 15C, Part III, European Physical Society (1991) 141.

Circulating and Trapped Energetic Ions/Alpha Particles in Tokamaks, Rep. PPL-2789, Plasma Physics Laboratory, Princeton University, Princeton, NJ (1989); submitted to Phys. Rev. Lett.

[39] STRACHAN, J.D., Bull. Am. Phys. Soc. **36** (1991) 2447.
[40] CHENG, C.Z., Phys. Fluids B **3** (1991) 2463, and references therein.
[41] BIGLARI, H., CHEN, L., Phys. Rev. Lett. **67** (1991) 3681.